

## Skeletonized wave-equation $Q_s$ tomography using surface-waves

Jing Li\*, Gaurav Dutta†, Gerard T. Schuster\*.

\* Department of Earth Science and Engineering, King Abdullah University of Science and Technology, Thuwal, Saudi Arabia, 23955-6900.

† CGG, Houston, TX, USA.

### SUMMARY

We present a skeletonized inversion method that inverts surface-wave data for the  $Q_s$  quality factor. Similar to the inversion of dispersion curves for the S-wave velocity model, the complicated surface-wave arrivals are skeletonized as simpler data, namely the amplitude spectra of the windowed Rayleigh-wave arrivals. The optimal  $Q_s$  model is then found that minimizes the difference in the peak frequencies of the predicted and observed Rayleigh wave arrivals using a gradient-based wave-equation optimization method. Solutions to the viscoelastic wave-equation are used to compute the predicted Rayleigh-wave arrivals and the misfit gradient at every iteration. This procedure, denoted as wave-equation  $Q_s$  tomography (WQ<sub>s</sub>), does not require the assumption of a layered model and tends to have fast and robust convergence compared to Q full waveform inversion (Q-FWI). Numerical examples with synthetic and field data demonstrate that the WQ<sub>s</sub> method can accurately invert for a smoothed approximation to the subsurface  $Q_s$  distribution as long as the  $V_s$  model is known with sufficient accuracy.

### INTRODUCTION

Surface waves play an important role in the characterization of the near surface for earthquake, engineering and environmental studies. Inverting and imaging surface waves can be an effective means for characterizing the subsurface at different scales (Dasgupta and Clark, 1998; Xia et al., 1999; Lin et al., 2008; Li and Hanafy, 2016), and can be important for site response and seismic hazard studies. Since the surface waves are sensitive to the near-surface elastic properties, estimation of the surface-wave velocity  $V_s$  and quality factor  $Q_s$  are of significant interest in exploration and earthquake seismology (Xia, 2014).

The near-surface S-wave velocity model is usually estimated from the dispersion curves of the recorded surface-wave arrivals (Park et al., 1998). However, in a real dissipative media, the propagation of the surface waves is strongly influenced by elastic damping in the near-surface that results in increasing amplitude loss and attenuation of high frequencies with distance travelled. As a result, the dispersion curves are also sensitive to the near-surface  $Q_s$  variations. He et al. (2015) showed that the phase velocity of the fundamental mode of the Rayleigh waves increases with decreasing values of  $Q_s$ . Thus, inverting dispersion curves for the S-wave velocity without taking into consideration the effect of  $Q_s$  can lead to erroneous estimates of the near-surface S-velocity distribution. Groos et al. (2014) showed that the S-wave velocity tomograms ob-

tained from elastic full waveform inversion (FWI) of Rayleigh waves have lower resolution when compared to the tomograms obtained by viscoelastic FWI when the near-surface is strongly anelastic. The increased resolution in S-wave tomograms obtained by taking into account the effect of  $Q_s$  can be useful in delineating near-surface faults or local anomalies (Pinson et al., 2008).

In this paper, we present a novel wave-equation  $Q_s$  tomography method (WQ<sub>s</sub>) that inverts skeletonized surface waves for the quality factor  $Q_s$ . The skeletonized data are the frequency shifts of the observed and predicted surface-wave's spectral peaks. The  $Q_s$  method is similar to the wave-equation  $Q_p$  inversion developed by Dutta (2016) and Dutta and Schuster (2016), except it inverts for  $Q_s$  from surface waves rather than  $Q_p$  from body-wave arrivals. The  $Q_s$  model is then found that minimizes the squared differences between the predicted and observed peak-frequency shifts associated with the Rayleigh wave arrivals. For this method, the isotropic viscoelastic wave equation based on the standard linear solid model (Robertsson et al., 1994) is used to generate the predicted Rayleigh-wave arrivals. The adjoint viscoelastic wave-equation is then used to backpropagate the residual traces that are obtained by weighting the observed Rayleigh-wave arrivals with their corresponding frequency shifts. The gradient for WQ<sub>s</sub> can be interpreted as the zero-lag cross-correlation between the forward propagated source wavefield and the backprojected weighted residual wavefield. Numerical examples on synthetic and field data validate the effectiveness of the proposed approach.

### THEORY OF WAVE-EQUATION $Q_s$ SKELETONIZED INVERSION

The theory of WQ<sub>s</sub> is derived in a manner that is similar to that for wave-equation traveltime inversion (Luo and Schuster, 1991) and surface-wave dispersion inversion (Li and Schuster, 2016; Li et al., 2017b). These steps include: (1) define a frequency-shift misfit function, (2) define a connective function that connects the frequency-shift residual of the Rayleigh-wave arrivals with the particle velocity seismograms, and (3) derive the gradient of the misfit function with respect to  $Q_s$  using the isotropic viscoelastic wave equation and the connective function in step (2).

In our analysis, we assume that the wave propagation honors the 2D isotropic viscoelastic equations of motion based on the standard linear solid (SLS) mechanism (Robertsson et al.,

## WQs Tomography

1994):

$$\begin{aligned}
 \rho \frac{\partial u}{\partial t} &= \frac{\partial \sigma_{xx}}{\partial x} + \frac{\partial \sigma_{xz}}{\partial z}, \\
 \rho \frac{\partial w}{\partial t} &= \frac{\partial \sigma_{zx}}{\partial x} + \frac{\partial \sigma_{zz}}{\partial z}, \\
 \frac{\partial \sigma_{xx}}{\partial t} &= \pi \frac{\tau_\epsilon^p}{\tau_\sigma} \left( \frac{\partial u}{\partial x} + \frac{\partial w}{\partial z} \right) - 2\mu \frac{\tau_\epsilon^s}{\tau_\sigma} \frac{\partial w}{\partial z} + r_{xx} + S_{xx}, \\
 \frac{\partial \sigma_{zz}}{\partial t} &= \pi \frac{\tau_\epsilon^p}{\tau_\sigma} \left( \frac{\partial u}{\partial x} + \frac{\partial w}{\partial z} \right) - 2\mu \frac{\tau_\epsilon^s}{\tau_\sigma} \frac{\partial u}{\partial x} + r_{zz} + S_{zz}, \\
 \frac{\partial \sigma_{xz}}{\partial t} &= \mu \frac{\tau_\epsilon^s}{\tau_\sigma} \left( \frac{\partial w}{\partial x} + \frac{\partial u}{\partial z} \right) + r_{xz}, \\
 \frac{\partial r_{xx}}{\partial t} &= -\frac{1}{\tau_\sigma} (r_{xx} + \pi \left( \frac{\tau_\epsilon^p}{\tau_\sigma} - 1 \right) \left( \frac{\partial u}{\partial x} + \frac{\partial w}{\partial z} \right) - 2\mu \left( \frac{\tau_\epsilon^s}{\tau_\sigma} - 1 \right) \frac{\partial w}{\partial z}), \\
 \frac{\partial r_{zz}}{\partial t} &= -\frac{1}{\tau_\sigma} (r_{zz} + \pi \left( \frac{\tau_\epsilon^p}{\tau_\sigma} - 1 \right) \left( \frac{\partial u}{\partial x} + \frac{\partial w}{\partial z} \right) - 2\mu \left( \frac{\tau_\epsilon^s}{\tau_\sigma} - 1 \right) \frac{\partial u}{\partial x}), \\
 \frac{\partial r_{xz}}{\partial t} &= -\frac{1}{\tau_\sigma} (r_{xz} + \mu \left( \frac{\tau_\epsilon^s}{\tau_\sigma} - 1 \right) \left( \frac{\partial u}{\partial z} + \frac{\partial w}{\partial x} \right)). \quad (1)
 \end{aligned}$$

Here,  $u$  and  $w$  are the horizontal- and vertical-particle-velocity components, respectively,  $\sigma_{ij}$  denotes the  $ij$ -th component of the symmetric stress tensor,  $r_{ij}$  is the memory variable,  $\tau_\epsilon^p$  and  $\tau_\epsilon^s$  are the strain relaxation times for the P and SV waves, respectively, and  $\tau_\sigma$  is the stress relaxation time for both the P and SV waves.  $S_{xx}$  and  $S_{zz}$  denote the source wavelets for the special case of an explosive source. The variable  $\pi = \lambda + 2\mu$  is related to the Lamé parameters  $\lambda$  and  $\mu$  whereas the stress and strain relaxation times are related to the quality factors  $Q_p$  and  $Q_s$  and the reference angular frequency  $\omega$  as (Carcione et al., 1988):

$$\begin{aligned}
 \tau_\sigma &= \frac{\sqrt{1 + \frac{1}{Q_p^2}} - \frac{1}{Q_p}}{\omega}, \\
 \tau_\epsilon^s &= \frac{1 + \omega Q_s \tau_\sigma}{\omega Q_s - \omega^2 \tau_\sigma}, \\
 \tau_\epsilon^p &= \frac{1}{\omega^2 \tau_\sigma}. \quad (2)
 \end{aligned}$$

Equation 1 is solved for a point source at each shot point by an O(2,4) time-space domain staggered grid finite-difference algorithm. In order to generate surface waves, an explicit free-surface boundary condition is implemented by using the mirroring technique proposed by Levander (1988).

It is possible to approximate a frequency independent seismic quality factor in a limited frequency range. We define the frequency-independent parameter  $\eta$  as:

$$\eta = \frac{\tau_\epsilon^s}{\tau_\sigma} - 1 = \frac{1 + (\sqrt{1 + \frac{1}{Q_p^2}} - \frac{1}{Q_p})^2}{(\sqrt{1 + \frac{1}{Q_p^2}} - \frac{1}{Q_p})[Q_s - (\sqrt{1 + \frac{1}{Q_p^2}} - \frac{1}{Q_p})]}. \quad (3)$$

For the parametrization in WQs,  $\eta$  is used because it is quite sensitive to small changes in  $Q_s$ . The relaxation ratio  $\eta$  is inverted at each iteration and the updates in  $\eta$  are then mapped to  $Q_s$  using equation 3.

### Misfit Function

We denote the Rayleigh-wave arrivals that are extracted from

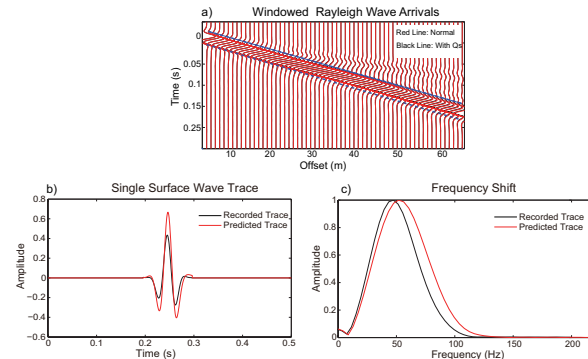


Figure 1: (a) A common shot gather (CSG) comparing the Rayleigh-wave arrivals with and without  $Q_s$ . The blue dashed line shows the window used to extract these arrivals for WQs, (b) comparison between a predicted and an observed surface-wave arrival, and (c) comparison between their amplitude spectra.

the recorded data as  $D_{f_g^{obs}}(\mathbf{g}, t; \mathbf{s})^{obs}$  for a vertical-component point source at  $\mathbf{s}$  and a vertical-component receiver at  $\mathbf{g}$  (the black curve in Figure 1a). The predicted Rayleigh-wave arrivals for the same source-receiver pair are denoted by  $D_{f_g^{pred}}(\mathbf{g}, t; \mathbf{s})^{pred}$  (the red curve in Figure 1a). The peak frequency of the observed and predicted spectra are denoted as  $f_g^{obs}$  and  $f_g^{pred}$ , respectively. Here,  $f_g^{pred} = f$  and  $f_g^{obs} = f - f_1$ , where  $f$  is the peak frequency of the event and  $f_1$  is the shift between the peak frequencies of the predicted and the observed traces due to  $Q_s$ . A comparison between the windowed observed and predicted Rayleigh-wave arrivals for a given  $Q_s$  model is shown in Figure 1b. The amplitude spectra of these arrivals are plotted in Figure 1c, where it is evident that the observed spectrum has a lower peak frequency than the predicted spectrum. The peak frequencies in these spectra are denoted as the skeletonized surface-wave data.

The goal of WQs is to find the attenuation model  $Q_s = F(\eta(\mathbf{x}))^{-1}$  so that  $f_g^{pred} \approx f_g^{obs}$  for all the traces. In our case, we use the frequency-shift residual  $\Delta f = f_g^{pred} - f_g^{obs}$  to form the skeletonized misfit function:

$$\varepsilon = \frac{1}{2} \sum_s \sum_g \Delta f(\mathbf{g}, \mathbf{s})^2. \quad (4)$$

The gradient  $\gamma(\mathbf{x})$  is given by

$$\gamma(\mathbf{x}) = \frac{\partial \varepsilon}{\partial \eta(\mathbf{x})} = \sum_s \sum_g \frac{\partial \Delta f}{\partial \eta(\mathbf{x})} \Delta f(\mathbf{g}, \mathbf{s}). \quad (5)$$

The  $\eta$  model is updated at each iteration using the iterative steepest descent method:

$$\eta^{(k+1)} = \eta^{(k)} - \alpha \overbrace{\sum_s \sum_g \frac{\partial \Delta f}{\partial \eta(\mathbf{x})} \Delta f(\mathbf{g}, \mathbf{s})}^{\gamma(\mathbf{x})=gradient}, \quad (6)$$

where  $\alpha$  is the step-length at the  $k$ -th iteration (Nocedal and Wright, 1999). The update for the relaxation ratio  $\eta$  is then mapped to  $Q_s$  using equation 3.

## WQs Tomography

### Connective Function

To find an analytic expression for the Fréchet derivative  $\frac{\partial \Delta f}{\partial \eta(\mathbf{x})}$  in equation 6, we define the connective function  $\Phi(\mathbf{g}, t; \mathbf{s})$  that connects the change in peak frequency of an arrival with the observed and the predicted Rayleigh-wave arrivals in Figure 1b as:

$$\Phi_{f_1}(\mathbf{g}, t; \mathbf{s}) = \int D_f(\mathbf{g}, t; \mathbf{s}) D_{f-f_1}(\mathbf{g}, t; \mathbf{s})^{obs} dt. \quad (7)$$

We seek an optimal  $Q_s$  model that minimizes the peak-frequency shift between an observed and a predicted trace. For an accurate background  $Q_s$  model, the predicted and the observed arrivals will have the same peak frequency. So, we define  $f_1 = \Delta f$  to be the frequency shift associated with the actual background  $Q_s$  model. If  $\Delta f = 0$ , it indicates that the correct background  $Q_s$  model has been found and the transmission surface-wave arrivals in the predicted and observed traces have the same peak frequencies. The derivative of  $\Phi_{f_1}$  with respect to  $f_1$  should be zero at the frequency-shift value  $f_1 = \Delta f$ , i.e.,

$$\begin{aligned} \dot{\Phi}_{\Delta f}(\Delta f, \eta(\mathbf{x})) &= \left[ \frac{\partial \Phi_{f_1}(\mathbf{g}, t; \mathbf{s})}{\partial f_1} \right]_{f_1=\Delta f} \\ &= \int D_f(\mathbf{g}, t; \mathbf{s}) \dot{D}_{f-\Delta f}(\mathbf{g}, t; \mathbf{s})^{obs} dt = 0, \end{aligned} \quad (8)$$

where  $\dot{D}_{f-\Delta f}(\mathbf{g}, t; \mathbf{s})^{obs} = [\partial D_{f-f_1}(\mathbf{g}, t; \mathbf{s})^{obs} / \partial f_1]_{f_1=\Delta f}$ . Note that  $\Delta f = 0$  if the predicted  $Q_s$  model is the actual  $Q_s$  model. Equation 8 is the connective function (Luo and Schuster, 1991) that connects the skeletonized data, i.e., the frequency-shift residuals of the Rayleigh-wave arrivals, with the particle-velocity seismograms. Such a connective function is required because there is no wave equation that relates the skeletonized data to a single type of model parameter (Dutta and Schuster, 2016).

Using the implicit function theorem and the connective function in equation 8, the Fréchet derivative with respect to the relaxation ratio  $\eta(\mathbf{x})$  can be expressed as

$$\frac{\partial \Delta f}{\partial \eta(\mathbf{x})} = - \frac{\partial \dot{\Phi}}{\partial \eta(\mathbf{x})} / \frac{\partial \dot{\Phi}}{\partial \Delta f}, \quad (9)$$

where the numerator on the right-hand side is given by

$$\frac{\partial \dot{\Phi}_{\Delta f}}{\partial \eta(\mathbf{x})} = \int \frac{\partial D_f(\mathbf{g}, t; \mathbf{s})}{\partial \eta(\mathbf{x})} \dot{D}_{f-\Delta f}(\mathbf{g}, t; \mathbf{s})^{obs} dt, \quad (10)$$

and the denominator by

$$\frac{\partial \dot{\Phi}_{\Delta f}}{\partial \Delta f} = \int D_f(\mathbf{g}, t; \mathbf{s}) \ddot{D}_{f-\Delta f}(\mathbf{g}, t; \mathbf{s})^{obs} dt = K_2. \quad (11)$$

Using equation 9, the gradient in equation 5 can be written as

$$\gamma(\mathbf{x}) = \frac{\partial \varepsilon}{\partial \eta(\mathbf{x})} = - \sum_s \sum_g \frac{\partial \dot{\Phi}}{\partial \eta(\mathbf{x})} \frac{\partial \dot{\Phi}}{\partial \Delta f} \Delta f(\mathbf{g}, \mathbf{s}). \quad (12)$$

Then, we use the adjoint-state method to derive the Fréchet derivative. Combining equations 10-12, the gradient for WQs

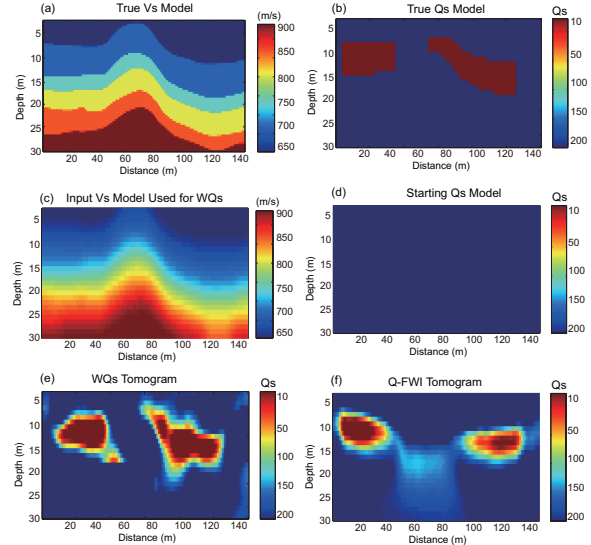


Figure 2: (a) True velocity and (b)  $Q_s$  models used for generating the observed data, (c) background  $V_s$  model used for WQs inversion, (d) starting  $Q_s$  model, (e) the  $Q_s$  tomogram computed by WQs, and (f) the  $Q_s$  tomogram computed by Q-FWI.

can be written as

$$\begin{aligned} \gamma(\mathbf{x}) &= - \sum_s \sum_g \frac{1}{K_2} \frac{\partial \dot{\Phi}}{\partial \eta(\mathbf{x})} \Delta f, \\ &= - \sum_s \int (2\mu \frac{\partial w}{\partial z} \hat{\sigma}_{xx} + 2\mu \frac{\partial u}{\partial x} \hat{\sigma}_{zz} - (\mu \frac{\partial u}{\partial z} + \mu \frac{\partial w}{\partial x}) \hat{\sigma}_{xz} \\ &\quad - 2\mu E \frac{\partial w}{\partial z} \hat{r}_{xx} - 2\mu E \frac{\partial u}{\partial x} \hat{r}_{zz} + \mu E (\frac{\partial w}{\partial x} + \frac{\partial u}{\partial z}) \hat{r}_{xz}) dt. \end{aligned} \quad (13)$$

Here  $(\hat{u}, \hat{w}, \hat{\sigma}_{xx}, \hat{\sigma}_{zz}, \hat{\sigma}_{xz}, \hat{r}_{xx}, \hat{r}_{zz}, \hat{r}_{xz})$  are the adjoint-state variables of  $(u, w, \sigma_{xx}, \sigma_{zz}, \sigma_{xz}, r_{xx}, r_{zz}, r_{xz})$ ,  $E = \frac{1}{\tau_0}$  and  $K_2$  is defined in equation 11. It can be shown that the residual trace,  $\hat{f}_w$ , that is backpropagated at every iteration is given by:

$$\hat{f}_w = \frac{1}{K_2} \dot{D}(\mathbf{g}, t; \mathbf{s})^{obs} \Delta f(\mathbf{g}, \mathbf{s}). \quad (14)$$

## NUMERICAL TESTS

We now compare the performance of WQs against that of Q-FWI for the near-surface  $V_s$  and  $Q_s$  models shown in Figure 2. A smooth version of the true S-wave velocity model, shown in Figure 2c, is used as the background velocity model for WQs and Q-FWI. The grid spacing and time sampling intervals for the 2D viscoelastic finite-difference algorithm are 1 m and 0.025 ms, respectively, and the center frequency of the source wavelet is 35 Hz. The observed data are generated by 40 shots evenly distributed on the surface and the data are recorded by 70 receivers every 2 m on the surface. The initial  $Q_s$  model is a homogeneous half space (Figure 2d).

The  $Q_s$  tomograms from the WQs and Q-FWI methods after 21 iterations are shown in Figures 2e and 2f, respectively. Figure

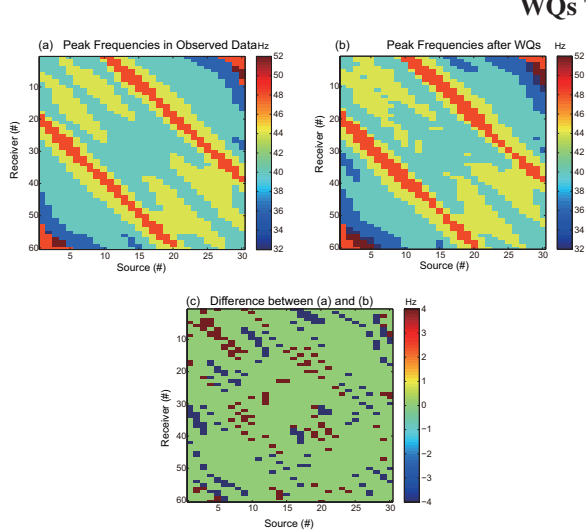


Figure 3: The peak-frequencies for different source-receiver pairs in (a) the observed data, (b) the predicted data after  $WQ_s$ , and (c) their differences.

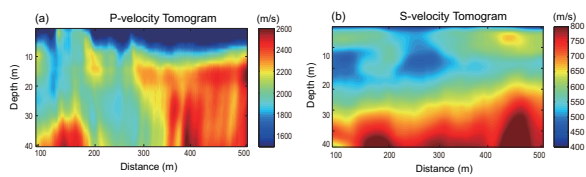


Figure 4: (a) P-wave tomogram with ray tracing tomography, and (b) S-wave velocity tomogram by wave equation dispersion inversion (Li et al., 2017a).

3 reveals that the predicted peak frequencies from  $WQ_s$  are very close to the actual ones for many source-receiver pairs.

The  $WQ_s$  method is now tested on a near-surface field data set recorded over the Qademah fault. There are 60 shots and 60 receivers on the surface placed at 10 m intervals. The first-arrival traveltimes are picked in all the CSGs and inverted using ray-based traveltimes tomography to obtain the P-wave velocity model shown in Figure 4a. The S-wave tomogram is shown in Figure 4b, which is obtained using the wave-equation surface wave dispersion method (Li et al., 2017b). These velocity models are used as the background velocity models for  $WQ_s$ . For  $WQ_s$ , the starting  $Q_s$  model is taken to be homogeneous with  $Q_s = 1000$  and the inverted  $Q_s$  tomogram is shown in Figure 5a. There is reasonable geological agreement between the S-wave velocity model in Figure 4b and the  $Q_s$  tomogram in Figure 5a. The high attenuation regions in the  $Q_s$  tomogram (low  $Q_s$  values) correspond to the low S-wave velocity regions. Previous work by Zhang et al. (2015) demonstrated that areas with high  $V_p/V_s$  ratios tend to have low  $Q$  values (or high attenuation). We calculate the  $V_p/V_s$  ratio using the tomograms in Figure 4 and the ratio is shown in Figure 5b. It can be seen from this figure that areas with high  $V_p/V_s$  ratio have low  $Q_s$  values.

As a final sanity check, the inverted  $Q_s$  tomogram is compared

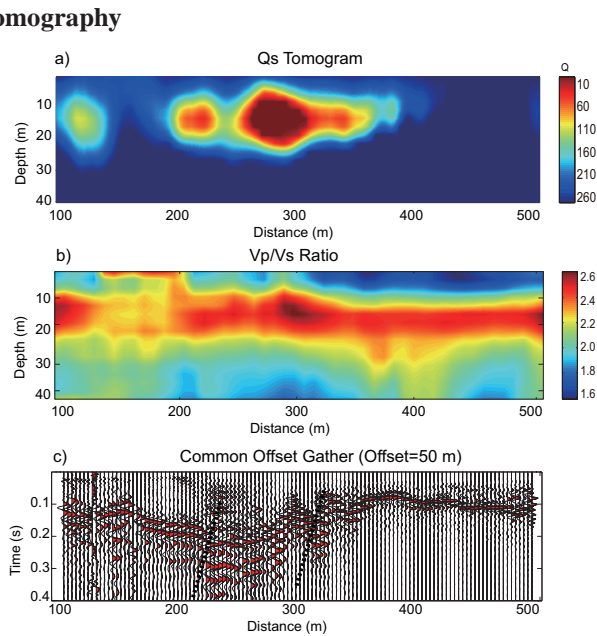


Figure 5: (a)  $WQ_s$  tomogram, (b) ratio ( $V_p/V_s$ ) computed from a) and b), and (c) common offset gather (offset=50 m) profile after data processing.

to a common offset gather (COG) profile (Hanafy et al., 2015). Figure 5c shows a COG profile using the processed data for an offset of 50 m. The black dashed line in this figure shows the location of the fault which is between 250-300 m. The locations of the  $Q_s$  anomalies in the  $WQ_s$  tomogram and the low-velocity area in the S-wave tomogram are consistent with the location of the fault, as indicated in the COG profile.

## CONCLUSIONS

We presented a skeletonized surface-wave wave-equation  $Q_s$  inversion method, where a  $Q_s$  model is found that minimizes the sum of the squared difference squared differences in the peak-frequencies of the observed and the predicted surface-wave arrivals. The gradient for  $WQ_s$  is obtained by a zero-lag cross-correlation between the forward propagated viscoelastic source wavefield and the weighted backprojected residuals that are obtained by weighting the observed particle velocity seismograms with the residual frequency shifts. This method does not require a layered-medium assumption used in conventional  $Q_s$  estimation techniques and also does not suffer from the limitations of ray-tracing based  $Q$  tomography methods or  $Q$ -FWI.

## EDITED REFERENCES

Note: This reference list is a copyedited version of the reference list submitted by the author. Reference lists for the 2017 SEG Technical Program Expanded Abstracts have been copyedited so that references provided with the online metadata for each paper will achieve a high degree of linking to cited sources that appear on the Web.

## REFERENCES

Carcione, J. M., D. Kosloff, and R. Kosloff, 1988, Wave propagation simulation in a linear viscoelastic medium: *Geophysical Journal International*, **95**, 597–611, <http://dx.doi.org/10.10111/j.1365-246X.1988.tb06706.x>.

Dasgupta, R. and R. A. Clark, 1998, Estimation of Q from surface seismic reflection data: *Geophysics*, **63**, 2120–2128, <http://dx.doi.org/10.1190/1.1444505>.

Dutta, G., 2016, Skeletonized wave-equation inversion for Q: 86th Annual International Meeting, SEG, Expanded Abstracts, 3618–3623, <http://dx.doi.org/10.1190/segam2016-13839306>.

Dutta, G. and G. T. Schuster, 2016, Wave-equation Q tomography: *Geophysics*, **81**, no. 6, R471–R484, <http://dx.doi.org/10.1190/geo2016-0081.1>.

Groos, L., M. Schäfer, T. Forbriger, and T. Bohlen, 2014, The role of attenuation in 2D full-waveform inversion of shallow-seismic body and Rayleigh waves: *Geophysics*, **79**, no. 6, R247–R261, <http://dx.doi.org/10.1190/geo2013-0462.1>.

Hanafy, S. M., A. AlTheyab, and G. T. Schuster, 2015, Controlled noise seismology: 85th Annual International Meeting, SEG, Expanded Abstracts, 5102–5106, <http://dx.doi.org/10.1190/segam2015-5906063.1>.

He, Y., J. Gao, and Z. Chen, 2015, On the comparison of properties of Rayleigh waves in elastic and viscoelastic media: *International Journal of Numerical Analysis and Modeling*, **12**, 254–267.

Levander, A. R., 1988, Fourth-order finite-difference P-SV seismograms: *Geophysics*, **53**, 1425–1436, <http://dx.doi.org/10.1190/1.1442422>.

Li, J., G. Dutta, and G. T. Schuster, 2017a, Wave-equation Qs inversion of skeletonized surface waves: *Geophysical Journal International*, **209**, 979–991, <https://doi.org/10.1093/gji/ggx051>.

Li, J., Z. Feng, and G. Schuster, 2017b, Wave-equation dispersion inversion: *Geophysical Journal International*, **208**, 1567–1578, <https://doi.org/10.1093/gji/ggw465>.

Li, J. and S. Hanafy, 2016, Skeletonized inversion of surface wave: Active source versus controlled noise comparison: *Interpretation*, **4**, SH11–SH19, <http://dx.doi.org/10.1190/INT-2015-0174.1>.

Li, J. and G. Schuster, 2016, Skeletonized wave-equation of surface wave dispersion inversion: 86th Annual International Meeting, SEG, Expanded Abstracts, 3630–3635, <http://dx.doi.org/10.1190/segam2016-13770057.1>.

Lin, F.-C., M. P. Moschetti, and M. H. Ritzwoller, 2008, Surface wave tomography of the Western United States from ambient seismic noise: Rayleigh and Love wave phase velocity maps: *Geophysical Journal International*, **173**, 281–298, <http://dx.doi.org/10.1111/j.1365-246X.2008.03720.x>.

Luo, Y. and G. T. Schuster, 1991, Wave-equation traveltime inversion: *Geophysics*, **56**, 645–653, <http://dx.doi.org/10.1190/1.1443081>.

Nocedal, J. and S. Wright, 1999, Numerical optimization: Springer Series in Operations Research, Springer Company 35.

Park, C. B., R. D. Miller, and J. Xia, 1998, Imaging dispersion curves of surface waves on multi-channel record: 68th Annual International Meeting, SEG, Expanded Abstracts, 1377–1380, <http://dx.doi.org/10.1190/1.1820161>.

Pinson, L. J., T. J. Henstock, J. K. Dix, and J. M. Bull, 2008, Estimating quality factor and mean grain size of sediments from high-resolution marine seismic data: *Geophysics*, **73**, no. 4, G19–G28, <http://dx.doi.org/10.1190/1.2937171>.

Robertsson, J. O., J. O. Blanch, and W. W. Symes, 1994, Viscoelastic finite-difference modeling: *Geophysics*, **59**, 1444–1456, <http://dx.doi.org/10.1190/1.1443701>.

Xia, J., 2014, Estimation of near-surface shear-wave velocities and quality factors using multichannel analysis of surface-wave methods: *Journal of Applied Geophysics*, **103**, 140–151, <http://dx.doi.org/10.1016/j.jappgeo.2014.01.016>.

Xia, J., R. D. Miller, and C. B. Park, 1999, Estimation of near-surface shear-wave velocity by inversion of Rayleigh waves: *Geophysics*, **64**, 691–700, <http://dx.doi.org/10.1190/1.1444578>.

Zhang, L., D. Zhu, and X. Zhang, 2015, Seismic attributes method for prediction of unconsolidated sand reservoirs of heavy oil: *The Open Fuels & Energy Science Journal*, **8**, 14–18, <http://dx.doi.org/10.2174/1876973X01508010014>.